Revisiting spin-state crossover in (MgFe)O by means of high-resolution x-ray diffraction from a single crystal

Konstantin Glazyrin,[1,*] Saiana Khandarkhaeva,[2] Leonid Dubrovinsky,[2] and Michael Sprung[1]
[1]*Photon Sciences, Deutsches Elektronen Synchrotron (DESY), 22607, Hamburg, Germany*
[2]*Bayerisches Geoinstitut, University of Bayreuth, Bayreuth, 95440, Germany*

(Received 22 December 2019; revised manuscript received 31 March 2020; accepted 1 April 2020; published 15 May 2020)

(MgFe)O is a solid solution with ferrous iron undergoing high to low spin state (HS-LS) crossover under high pressure. The exact state of the material in the region of the crossover is still a mystery as domains with different spin states may coexist over a wide pressure range without changing the crystal structure neither in terms of symmetry nor in terms of the atomic positions. At the conditions of the crossover, (MgFe)O is a special type of microscopic disorder system. We explore the influences of: (a) stress-strain relations in a diamond-anvil cell, (b) time-relaxation processes, and (c) the crossover itself on the characteristic features of a single-crystal $(111)_{hkl}$ Bragg spot across the transformation. Using high-resolution x-ray diffraction as a method for studies of unconventional processes at the conditions of suppressed diffusion, we detect and discuss subtle changes in the $(111)_{hkl}$ Bragg spot projections which we measure and analyze as a function of pressure. We report changes in the spot size which can be correlated with the HS-LS relative abundance. In addition, we report the formation of structural defects in a single crystal as an intrinsic material response to the HS-LS crossover. These static defects are formed and accumulated during the compression within the crossover pressure range.

DOI: 10.1103/PhysRevB.101.184203

I. INTRODUCTION

The solid-state solution MgO-FeO [or (Mg,Fe)O] may seem trivial, but it plays an important role for the lower mantle of the earth (and potential superearths) and exhibits a complex and at the same time fascinating behavior. The spin-state crossover of ferrous iron can, indeed, play an important role in natural processes of planetary scale. On one hand, the crossover affects elastic properties of the material. On the other hand, it may be involved in various diverse processes featuring multiple phases, e.g., involving iron partitioning in major constituents of geophysically and geochemically important mineral assemblages (earth's lower mantle, ultralow velocity zones, terrestrial planets in the solar system, and exoplanets, etc.) [1–4].

At the same time, we should not forget that (MgFe)O is an oxide system with a strong correlation between lattice and spins of iron. An extensive introduction of to the multifaceted complexity of transition-metal oxides can be found in Ref. [5] with examples of systems controlled by competing dominant states, which are often not spatially homogeneous. Here, we will focus more on the description of (MgFe)O as a strongly correlated system featuring (MgFe)O with low to moderate concentration of iron with $x_{\mathrm{Fe}} = 0.19(1)$. This material retains its cubic structure at all pressures relevant for the spin-state crossover.

The spin-state crossover in (MgFe)O is a complex thermodynamic quantum phenomenon [1,6,7]. There is a consensus in the existing literature that, during the crossover, the high and low spin states of ferrous iron coexist in the same cubic structure. The state of coexistence, in turn, should imply a creation of a spatially inhomogeneous disordered system with competing domains of Fe^{2+} in the high state (HS) and low state (LS). Review of the literature reflects the significant progress unraveling different important aspects of this phenomenon [1], and still most of the studies are focused on the properties of the bulk material. Thus, the phenomenon and the underlying system were never closely investigated on the submicron and nanoscales. After a careful consideration, it becomes clear that the origins can be found at the atomic level as we attempt to demonstrate below.

Within the pressure range of the spin-state crossover, (MgFe)O can be described as a "frustrated system." Although the total abundance of HS and LS domains is dictated by thermodynamic pressure and temperature conditions, the exact distribution of HS-LS domains should be free to change for a given thermodynamic point. Imagine that the system may switch a specific Fe^{2+}_{LS} to Fe^{2+}_{HS}, individually with or without a small temperature perturbation. However, the restraint on the spin-state abundance balance would require another Fe^{2+}_{HS} to switch into Fe^{2+}_{LS}, promoting a "breathing" of the system. The presence of competing but spatially heterogeneous dominant states could be described within the term of Griffiths phases, common for other transition element oxides (e.g., Refs. [8,9] and references within).

It is well documented that, in addition to pressure, the system is very sensitive to temperature. Temperature increase expands the pressure region of HS and LS coexistence [6,10].

*Corresponding author: konstantin.glazyrin@desy.de

Thus, even under conditions of a strongly suppressed diffusion of Mg and Fe at high pressure and ambient temperature [11], even small temperature fluctuations introduce an additional complication to the picture.

The description of (MgFe)O spin-state crossover as a "frustrated system" can be retranslated into a picture of system disorder. At the moment, we do not have any information about the equilibrium shapes, sizes, and the distribution of HS and LS domains. They may be small, down to nanoscale size. They could be still large enough (i.e., 10–100 of nanometers) that they would not create a significant detectable contribution to the conventional high-pressure powder [12] or single-crystal diffraction signal from individual spin states (Supplemental Material of Ref. [13]). What is important to understand is that these domains have significant contact strains, e.g., separating configurations with different spin states. The HS and LS domains of (Mg,Fe)O should have lower and higher densities, respectively, and, thus, their presence and competition introduce density fluctuations on the atomic scale (i.e., with a simplest picture of a single Fe^{2+}_{LS} surrounded by six Fe^{2+}_{HS}'s), which, in turn, lead to a complex strain field in the bulk of the material.

As an additional complication, we refer to publications exploring intrinsic variation of iron concentration inside (MgFe)O [13,14]. The experimental evidence suggests that iron cations tend to cluster forming inhomogeneous regions within the crystal matrix. A solid-state solution has a random distribution of impurity, and, in a contrast to homogenization, the randomization may, indeed, induce "clustering." Obviously, the latter effect also correlates with spin-state crossover and may be superimposed with other effects described above. All the mentioned observations indicate the complexity of spin-state crossover and highlight (MgFe)O as an intricate and an underexplored system.

X-ray diffraction is the natural methodological choice for investigations of material strain and related effects, caused, for example, by subtle processes, such as the spin-state crossover. Considering different contributions to the diffraction signal and harsh experimental environment in high-pressure diamond-anvil cell (DAC) experiments, the sought information can only be provided from a single crystal of exceptional quality which should be preserved during the compression. In comparison with powder material, the single-crystal diffraction signal of (Mg,Fe)O should be free from additional undesirable microstrains unavoidably appearing in compressed powders (grain boundaries, grain-grain contacts, higher concentration of dislocations, etc.). Importantly, for any existing diffraction condition, single crystals provide the highest signal-to-noise ratio if we consider the same sample scattering volume.

In this paper, we investigate the effect of high pressure on (Mg,Fe)O single-crystal $(111)_{hkl}$ Bragg reflection by means of synchrotron-based x-ray diffraction. We take advantage of high resolution [controlled in our case by a combination of a long sample to detector distance (SDD) and an appropriate choice of x-ray energy] to monitor the effects of compression on the sample diffraction signal. We analyze the signal collected across the spin-state crossover. We pay special attention to a characterization of the disordered state (spin-state crossover) and, the material's response originating from effects on the nanoscale.

Our paper could also be considered important for other methodological reasons, particularly, for developments in the field of dynamic compression experiments using diamond-anvil cells. The findings presented below may provide references for analysis and comparison of the effects of the stresses and strains (and additional factors, such as relaxation processes) in relatively slow static and dynamic DAC experiments (membrane and piezodriven DACs).

II. EXPERIMENTAL DETAILS

(MgFe)O single crystals were synthesized at Bayerisches Geoinstitut, Bayreuth University. We used a crystal from the batch used in a previous study [13], and we refer to the iron concentration of $x_{\mathrm{Fe}} = 0.19(1)$.

A small crystal $(10 \times 15 \times 5\,\mu\mathrm{m}^3)$ was preselected at the P02.2 extreme conditions beamline [15], PETRA III, Deutsches Elektronen Synchrotron (DESY) using the energy of 42.7 keV. The sample was loaded into a symmetric DAC with an opening of 70° equipped with Boehler-Almax diamonds. We used Re as the gasket material, Ne as the pressure medium, a tiny piece of ruby (pressure marker), and a tiny piece of tungsten were placed inside the sample chamber. Tungsten was used for the alignment of the sample with respect to the x-ray beam and for the centering of the DAC with respect to the goniometer rotation axis (strong x-ray absorber). The diamond-anvil cell (x-ray aperture ±32°) was manually preoriented in such a way that (MgFe)O $(111)_{hkl}$ was located on the horizontal plane.

X-ray diffraction data at high resolution were collected at the P10 Coherence Applications Beamline, PETRA III, DESY (Fig. 1). The energy of 15 keV was selected by a Si(111) channel cut monochromator. We used a stack of compound refractive lenses located 1.6 m upstream from the sample in order to focus the x-ray beam down to $2.5 \times 4.5\,\mu\mathrm{m}^2$ (vertical × horizontal). The sample to detector distance was 5 m with a long flight path under vacuum installed on the horizontal plane between the sample and the Eiger X 4M detector (pixel size $75 \times 75\,\mu\mathrm{m}^2$). Bragg peak intensity was collected by rotating the sample along the φ axis of a goniometer (scanning of a Bragg spot on the horizontal plane). At 15 keV, we were efficiently measuring the sample absorption and used this signal for precision centering. The calibration of the 2θ range at different detector positions was performed by performing a cross correlation with the position of Au powder (particle size <100 nm) measured separately at ambient conditions and different detector positions. For this, we used a calibration by the position of Au $(111)_{hkl}$ collected at ambient conditions. Afterwards, the 2θ angle of the flight-path tube was fixed, we adjusted the position of the detector to enhance the coverage of the (MgFe)O $(111)_{hkl}$ Bragg spot by the detector. This was necessary due to the presence of intrinsic gaps of sensitive material within the detector sensitive area due to its modular design.

The choice of the Bragg reflection comes from the following consideration: The $(111)_{hkl}$ is the plane with the densest packing, and we could expect the strongest manifestation of the crossover; at the same time, this reflection is accessible

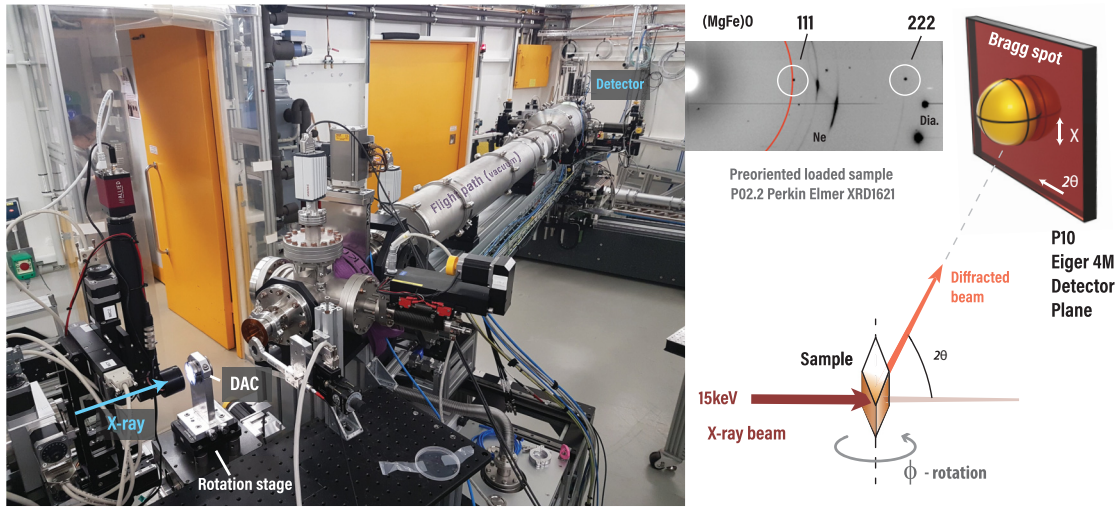

FIG. 1. (Left) A photograph of the high-resolution experimental setup of the P10 beamline with a diamond-anvil cell. (Right) A diagram supplementing the photograph indicating the geometry of the collection used in the paper. At a high-resolution regime of the beamline, we observe the three-dimensional (3D) shape of the Bragg peak as a function of 2θ, χ directions, and as a function of ϕ rotation. Using a two-dimensional (2D) pattern shown in the middle, we highlight the quality of the loaded and prealigned sample. The latter pattern was collected at the beamline P02.2 as a preparation step. Data were collected at a different energy in comparison to P10. We mark the Bragg reflections $(111)_{hkl}$ and $(222)_{hkl}$ and indicate additional scattering from the sample chamber (Ne pressure medium and diamond Bragg peaks).

through the aperture of a DAC for the given, rather low, energy of 15 keV.

We recorded the pressure dependence of the Bragg spot. At each pressure, we recorded data during scans of the ϕ axis (Fig. 1) and captured the Bragg spot in a step of 0.01°. Here and below, we will present and refer to the data as "integrated" (as a full sum of individual frames of a dataset resulting in a single data frame, thus, representing the full integral intensity of the Bragg spot, integrated over a range of ϕ) and as individual frames or "slices" (data collected at a specific ϕ position, representing an individual frame of the Bragg peak). An example comparing the difference between the slices and the integrated intensity at 72 GPa is provided in Fig. 2. We indicate the convention used for the analysis of the data recorded on the detector plane. Figures representing intensity variations as a function of 2θ and χ operate with data extracted from the integrated data. Determination of the Bragg spot size as a function of ϕ rotation is based on the data from individual slices. We use the latter to extract the Bragg spot intensity (a single value corresponding to a specific ϕ position) and the position of its center of mass (C.o.M) as a function of both 2θ and ϕ. An additional graphical representation can be found in Appendix A.

Figure 2 deserves additional clarification due to the presence of specific features appearing on the detector because of a partially coherent incident beam. The coherent fraction was significant enough that we can observe additional features in the form of interference fringes. The high intensity speckles shown in Fig. 2 indicate a strong inhomogeneity of scattered intensity both visible in integrated intensity and visible in individual slices. However, the coherent fraction used and the oversampling conditions did not allow to use phasing algorithms to fully reconstruct the sample. Indeed, the coherent beam fraction was not sufficient to affect either the main scattering signal of the measured Bragg spot as well as the integrated scattering signal.

We suggest that some of the features could be attributed to the high-pressure environment surrounding the sample. Indeed, the phase of the partially coherent x-ray beam can be modified across the sample environment in three different scenarios: before being scattered by the sample, upon the scattering from the sample, and during the further transmission downstream. During the process of transmission and scattering of the x-ray beam, certain features of a sample environment may contribute to the final Bragg spot in terms of weak intensity fringes. In certain conditions, the appearing fringes could be attributed to the shape of the sample, grain boundaries of materials with a strong scattering power, etc. Since the signals from the fringes are weak, they do not interfere with our analysis of the Bragg spot which we perform within the framework of conventional diffraction.

In the case of the current paper, we see a nice correspondence of the Ne grain boundaries (detected with visible light) with additional fringes appearing in the Bragg spot (Fig. 2, see also Fig. 9 of Appendix B). The contribution of Ne grains to the diffraction signal of (MgFe)O is highly probable. We note that Ne pressure medium has significant volume and strong scattering power. We also recall that Ne contribution to the (MgFe)O signal cannot be considered a diffraction signal from Ne itself, and in order to complete this discussion, we report that, after crystallization of Ne, its major grain boundaries remained at the same positions and changed only as far as could be expected from a conventional diamond-anvil cell experiment.

Before we present the results, we introduce the methodology of the data collection. By scanning the Bragg spot by means of the 2D detector and the ϕ-motorized rotation stage [see also Fig. 1 (Right) for clarification], we selected to trace the following practical parameters: center of mass and

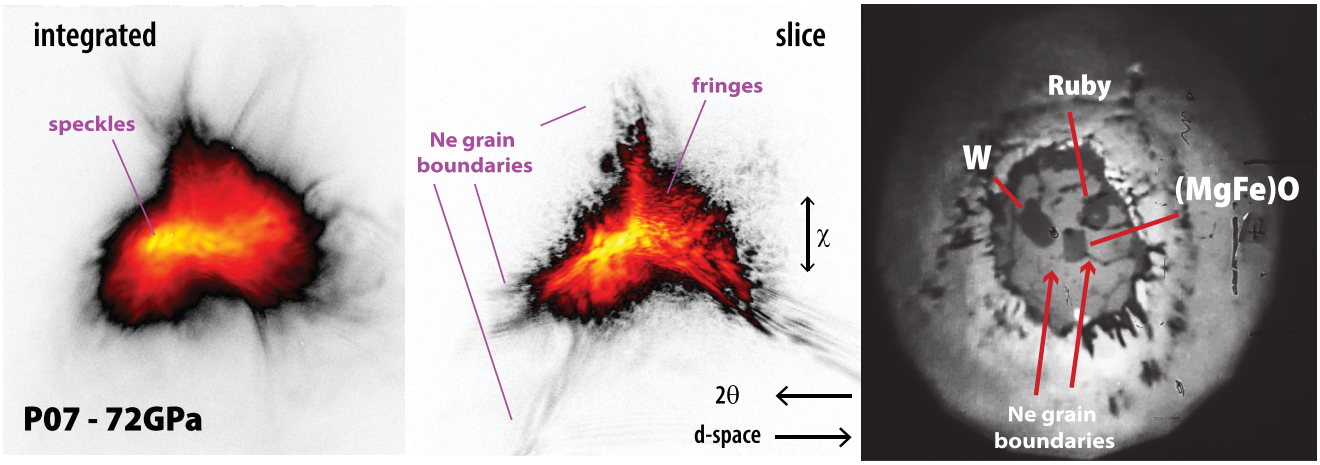

FIG. 2. Snapshots of the Bragg spot as captured by the detector and a photograph of the sample chamber at high pressure of 72 GPa. (Left) Integrated Bragg spot featuring the full intensity of the peak, integrated over a set of ϕ angles and an additional speckle structure. (Middle) Individual frame or a slice of the Bragg peak in the vicinity of the maximum intensity. We show the directions for the axes corresponding to the χ and 2θ angles. χ corresponds to the angle on the arc of the diffraction circle. We highlight the specific contributions to the Bragg spot including the speckles of high intensity and additional interference fringes of weak intensity due to the nonzero coherent fraction of the x-ray beam. (Right) The photograph of the sample chamber made using visible light (with indirect backlight illumination). The diamonds have 200-μm culet size. Note the striking resemblance of the Ne grain boundaries with the features on the snapshot in the middle.

maximum intensity positions of the Bragg spot peak (2θ angle or d spacing), width of the spot profile as projected on the arc of the diffraction cone (χ angle), and width of the spot profile as a function of ϕ rotation. Data on d-spacing values and widths of the peak on the detector plane perpendicular to the diffraction ring on the detector plane (along 2θ) represent the data on the experimental average stress conditions and strain. Data on the χ angle should produce information on the mosaicity of the crystal if it would be evolving under pressure, but it should not be considered being limited to this single parameter.

The size of the particular Bragg spot in the reciprocal and the direct space is affected by many parameters, including the instrument. In our case, it is a natural choice to use the width of the Bragg spot in units of χ and ϕ angle rotations to detect a trend of Bragg spot broadening due to an additional scattering contribution which could be attributed to the presence of spin-state disorder in the material across the crossover. As would be clear from the results, a single d spacing or 2θ projection is not enough for this purpose.

All of the results presented below correspond to an ambient temperature study. We expect similar effects for the regimes of higher and lower temperatures.

III. RESULTS

We collected x-ray diffraction data at several pressure points, covering the complete spin-state crossover as well as collecting information at lower pressures (Fig. 3). The resulting pressure-volume (P-V) relation is plotted together with reference equations of state (EOSes) for pure MgO.

In the inset of Fig. 3 we show the 2θ profile width of the integrated $(111)_{hkl}$ Bragg spot and illustrate our definition of the Bragg peak full width ($FW_{1/3}$), which we calculate here at 1/3 of the peak height (2θ and χ projections). Special definition of these parameters is necessary because the shape of the peak was asymmetric at all pressure points (effect of high-resolution x-ray diffraction). Due to the specific shape of the peak, for each pressure point, we present two values of the lattice parameter and the unit-cell volume—one for the center of the peak mass (open symbols in the figure)

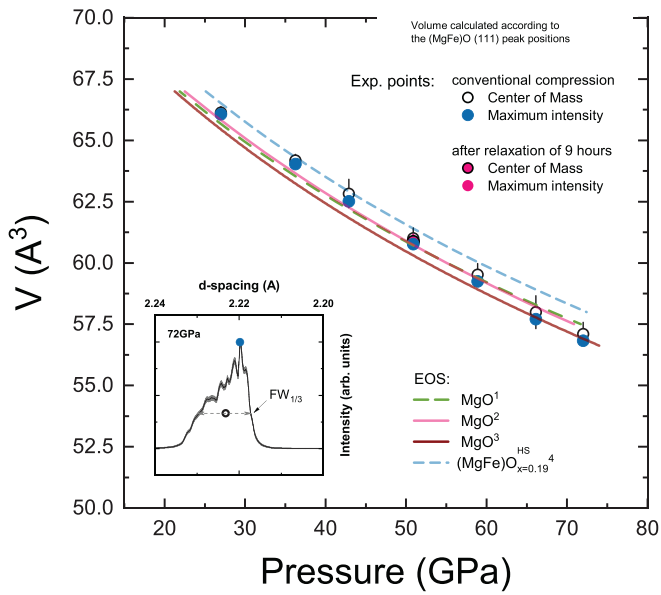

FIG. 3. Unit-cell volume as a function of pressure for our (MgFe)O material. The solid points correspond to the maximum intensity of a Bragg peak, whereas the open points correspond to the center of mass of the Bragg peak. The inset demonstrates a profile of the full integrated Bragg spot intensity as a function of d spacing. In order to capture the width of the peak in an optimal way, here, we define the full width at 1/3 of the peak height. For the guidelines, we use equation of states (EOS): 1 [16], 2 [17], 3 [18], and 4 [13] with the latter indicating the HS EOS.

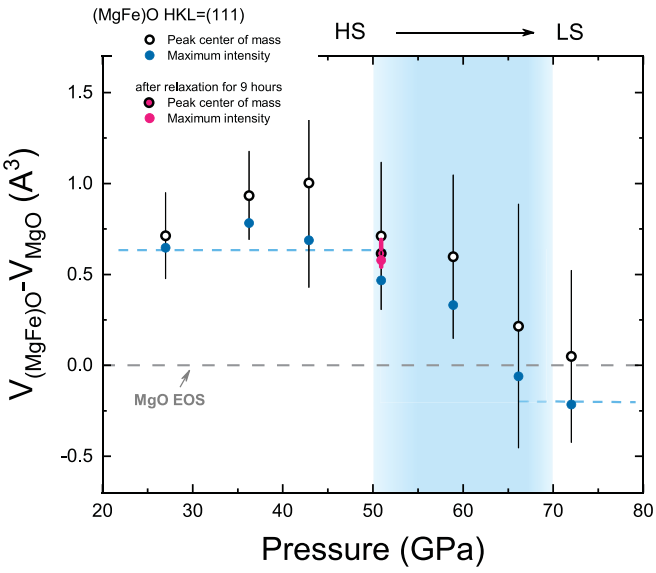

FIG. 4. Difference between (MgFe)O and MgO unit-cell volumes as a function of pressure. The open symbols were calculated using the Bragg peak center of mass, whereas the solid symbols were calculated using the maximum of the Bragg spot peak. The error bars represent the half-width at 1/3 of the Bragg peak width as introduced in Fig. 3. The MgO equation of states is taken from Ref. [18]. The dashed lines are the guidelines. The tentative region of the HS to LS crossover is indicated with the blue color.

and the position corresponding to the maximum intensity (solid symbols).

The unusually broad intensity profile of the peak in 2θ projection requires a separate clarification. It is true for most of the common 2D large area detectors used at popular high-pressure diffraction beamlines that their pixel size ranges from 144 to 200 μm (detectors with small sensitive areas, such as Mar165 or Lambda are not considered). Assuming a SDD equal to 400 mm and a conventional x-ray diffraction energy of 32–42keV, the projected width of the Bragg spot (integrated) would be, at maximum, three pixels for the highest width of the Bragg spot reported in this paper (at highest pressures). Thus, by the criteria commonly used in the high-pressure community, the data reported here were collected from the crystal of (MgFe)O of exceptional quality, which was preserved at all experimental points as is possible in a diamond-anvil cell high-pressure environment.

Going back to Fig. 3, we see that our data are in good agreement with the literature [16–18]. Considering previously reported equations of state for the pure MgO material, we note some inconsistencies among the existing literature with the strongest one related to nanosize MgO material [19]. Here and below, we will use the data of Jacobsen *et al.* [18] measured on similar material, namely, a small single crystal of MgO in He pressure medium at room temperature, which we consider as a reference EOS for bulk material.

In Fig. 4 we compare our *P*-*V* data with the equation of states for MgO by calculating a difference between unit-cell volume of our material and the unit-cell volume of MgO at the same pressures [18]. The region of spin-state crossover is clearly visible and agrees well with previous measurements [1,13,20].

Having confirmed the region of the spin-state crossover, we present the data describing the (MgFe)O $(111)_{hkl}$ Bragg peak shape using three cross sections, namely, using profiles collected in 2θ, χ projections, and a profile collected during ϕ rotation as was introduced above.

Before we continue our analysis, for a complete description of the data shown in Figs. 3 and 4, we will discuss the point of 51 GPa, which was measured twice. The reason for emphasizing this specific point originates from its vicinity to HS-LS crossover onset [13] for our specific composition of $x_{Fe} = 0.19(1)$. The first measurement corresponds to the time interval of 30–40 min after compression to the target value, and the next dataset was collected 9 h later ("relaxed"-pink symbols in figures). As one can already see from Fig. 5 featuring the 2θ cross section, the peak width of the relaxed point is much narrower if compared with the other points and indicates stress and strain relaxation in the sample chamber. These observations are also supported by the raw data displayed in Fig. 9 of Appendix B.

In Fig. 5, we can see that, apart from the obvious compression effect controlling the Bragg peak position and intensity distribution as a function 2θ (strongly asymmetric peak profile), it is really hard to spot a specific trend. Still, the relaxation effect at 51 GPa is quite obvious. One can clearly see that the width of the Bragg peak expressed in 2θ, or in convenient strain d-spacing units, became narrower indicating strain relaxation. The center-of-mass for this peak is moved to a higher d-spacing value by an insignificant value as illustrated in the same figure. At the same time, in contrast to the center-of-mass value, the maximum of the intensity moved to a lower d-spacing value. Since the positions for the center of mass and the maximum of intensity should have a strict relation with pressure dictated by the material equation of state (*P*-*V* relationship), we suggest that the strain relaxation is accompanied with stress relaxation effects in the sample chamber. Since the pressure measured using the ruby marker (external to the sample itself) has not changed within the error bars, we consider this observation as a typical manifestation of complex stress-strain conditions of the high-pressure environment—these effects are typically disregarded in many experiments, although they could be, quite important. Our observations clearly indicate that a physical system compressed in a diamond-anvil cell may require a significant amount of time to reach equilibrium, especially at conditions of suppressed kinetics. It may well be a longer period of time per point than is typically granted for diffraction beam times at large-scale synchrotron facilities.

Observations made for our particular sample may be applicable for any other sample compressed using diamond-anvil cells. Considering the width of the measured profiles in d-spacing units (Fig. 5), we observed significant strain evolution during the time interval following the mechanical compression and experimental equilibration. Although prior and after the 9 h of relaxation, the pressure was remaining almost the same (position of the Bragg peak center of mass and frequency of ruby fluorescence signal), we emphasize that the crystal had a specific strain distribution, and this distribution was much higher in the state preceding the

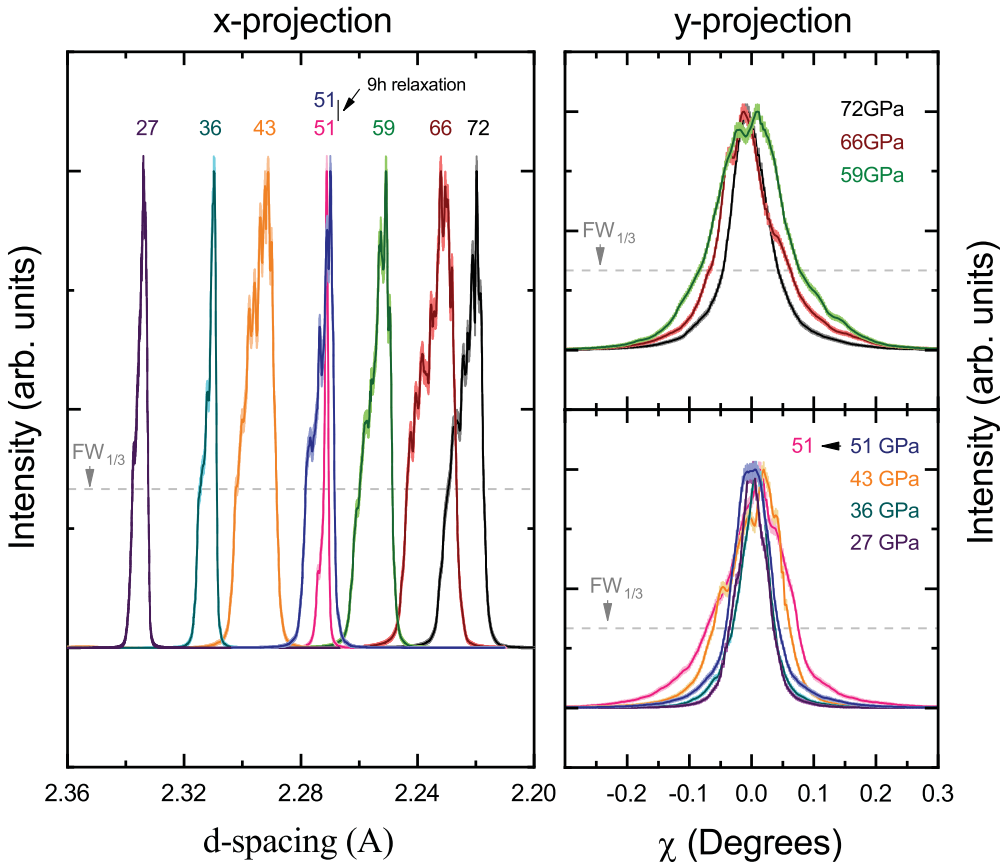

FIG. 5. Projections χ and 2θ of the Bragg spot on as a function of pressure. Intensities are normalized by the peak amplitude . The 2θ is represented in units of d spacing. (Left) The projection of the integrated Bragg peak on the 2θ axis slides to the direction of lower d-spacing values as a result of compression. We highlight the point of 51 GPa. This point was measured twice with 9 h between the measurements. After hours of relaxation, the width of the peak in 2θ has become narrower. Our observation indicates a complex stress-strain relaxation process. The 2θ position of the peak did not change significantly whereas the corresponding projection on χ increased after the relaxation period. (Right) The projection of the integrated Bragg peak on χ. The width of the peak in χ projection has increased upon entering the stability region of the spin-state crossover, but, then, it decreases as we compress further and complete the transition at 72 GPa.

relaxation. Although, in our experience, the exact values will strongly depend on sample size and other conditions related to compression, in our particular case, we report a change in 2θ projection width using relative d-spacing units ($\Delta d/d$ as the representation of the $FW_{1/32\theta}$ value normalized to the peak center of mass) from $\sim 4.5(4)^{-4}$ to $\sim 0.8(2)^{-4}$ for the cases preceding and following the relaxation, respectively. Here, we are assuming that relaxation processes appearing in the sample are an integral part of the sample environment, and we assume that the soft pressure medium, such as Ne, would have shorter relaxation times than the oxide system.

In the continuation of our discussion, the duration of relaxation depends on the parameter of temperature. The duration should decrease for higher and increase for lower temperatures, respectively. We indicate that compression suppresses diffusion substantially, and the higher the pressure, the longer a relaxation process will take for a given temperature. Considering the diffusion coefficient values for the Mg-Fe interdiffusion reported earlier (Supplemental Material of Ref. [13]), the temperature increase should be considerable.

Our observations indicate that ambient temperature dynamic compression experiments, which become more and more popular (i.e., Ref. [21]), may not reach a full equilibrium at the time of the compression, and their comparison with the static experiments should be performed carefully. Significant amount of strain accommodated during dynamic compression may divert the process from the equilibrium path. If one considers the example of (MgFe)O, any inhomogeneous strain on powders (i.e., directional) may promote local distortions of initially perfect FeO_6 octahedron (tetrahedral or rhombohedral distortions) and either trigger the transformation of HS into LS prematurely (Ref. [20]) or delay it. Indeed, the criterions for HS to LS transition for ferrous iron would be different depending on the distortion of local environment and the exact crystal-field configuration. Local strains at dynamic compression will regulate boundaries of the spin-state crossover stability field, and it may become intricate to control or characterize great number of parameters involved.

If we consider the projection along the χ direction, the broadening of the Bragg peak (Fig. 5) increases as we enter the region of the spin-state crossover at 51 GPa. The corresponding width value reaches maximum at about 59 GPa and then decreases, approaching the typical values preceding the HS-LS crossover at 72GPa.

It is inherently difficult to present and describe evolution of the 3D Bragg peak as a function of pressure, especially in the

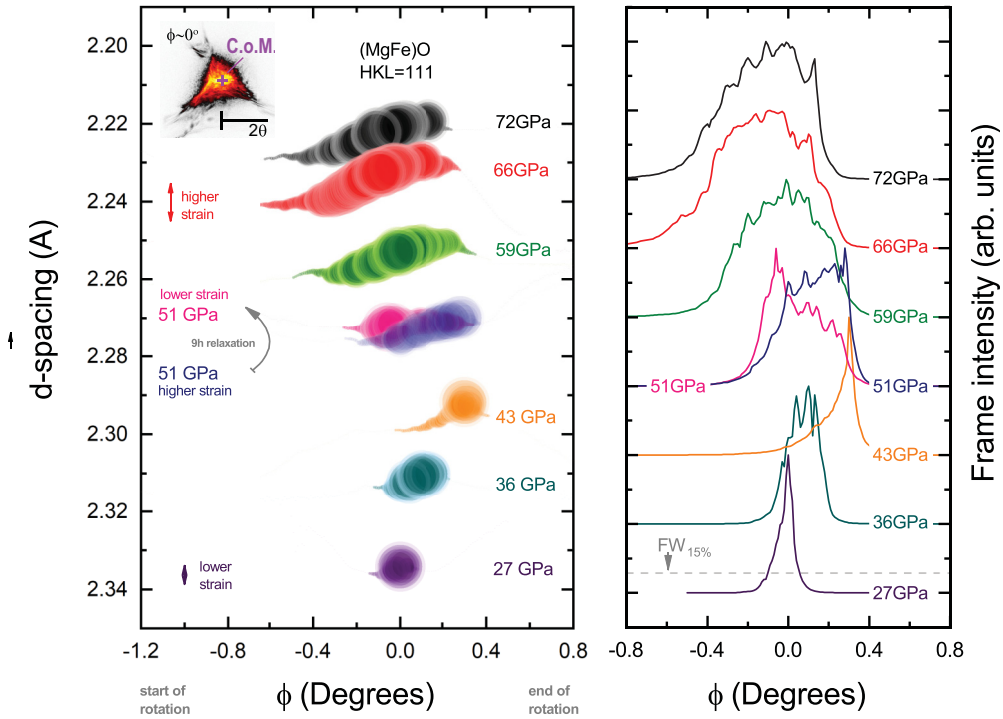

FIG. 6. (Right) Width of the Bragg spot in the direction perpendicular to the detector plane as a function of pressure. It is provided in the units of sample rotation along the ϕ axis. $FW_{15\%}\phi$ is estimated at 15% of the normalized peak amplitude. The value of ϕ in absolute values was different at each point, however, for the sake of comparative analysis and simplicity of representation, we set $\phi = 0^\circ$ close to the middle of the dataset. (Left) Intensity and 2θ position of the Bragg spot as a function of pressure and ϕ rotation. Data represent changes in intensity C.o.M. and its position measured as a function of ϕ rotation or a Bragg spot slice (see the inset). Larger and smaller spots indicate higher and lower intensities of the slice, respectively. The size of the points varies in linear scale as a function of the in-frame intensity, and they are shown in ascending sorting. Please note that the Bragg spot is not a simple ellipsoid but has a certain nontrivial 3D distribution of intensity in the reciprocal space. At a given Bragg spot slice, the C.o.M. of intensity changes its 2θ position as a function of ϕ rotation reflecting scattering from a single crystal. There is an obvious increase in the width and a change in Bragg spot shape within the spin-state crossover region. At lower pressures, we see stronger confinement of intensity, which is spread out at higher pressures and reaches maximum at 66 GPa.

situation when the Bragg peak shows additional interference effects (Fig. 2). On the right side of Fig. 6 we demonstrate the evolution of the $(111)_{hkl}$ width in the direction perpendicular to the detector plane. The peak profile measurement during the ϕ rotation could be introduced in the framework of ω-2θ scanning on conventional x-ray laboratory diffractometers equipped with a 2D detector instead of a point detector. Imagine, that a series of frames collected during ϕ rotation represent a set of data, and each frame corresponds to a slice of the Bragg spot. If we consider that each frame contains a 2D distribution of intensity attributed to the Bragg spot, within the same slice, we can find the intensity center as a function of ϕ and 2θ (intensity). We can also integrate the total intensity captured in the individual frame and parametrize it as a single value. This information should help with the interpretation of Fig. 6. Finally, here and below, in order to avoid any confusion and in order to have an optimal representation, we use a different notation for the $FW_{15\%\phi}$ of the peak, namely, the width measured at 15% of the height.

In Fig. 6, in the right panel, we see that the profile width increases as we approach the pressure of 51 GPa, and it then remains large up to 72GPa, namely, the pressure range corresponding to the end of the crossover. The left panel of Fig. 6 shows the 2θ position of intensity C.o.M. changing as a function of ϕ rotation and as a function of frame. Such a representation reflects the corresponding strain distribution in direct and reciprocal spaces. We recall the details of the scattering geometry by referencing Fig. 1 and the complementary illustration shown in Fig. 8 of Appendix A.

A careful inspection of Fig. 6 will indicate that the data corresponding to 43 GPa may have strange shapes. We consider that this point is a good example for an illustration that the compression is always a complex interplay between the strain and the other parameters in play in the tiny sample chamber containing even tinier samples, in turn, surrounded by quasihydrostatic solid pressure medium. This pressure point was collected according to exactly the same protocol as the other unrelaxed points. In addition, if we consider Fig. 9 (Appendix B), then we will find that the central slice of the Bragg peak center is not that different from the other pressure points.

We analyze different projections and their widths in the following section where we compare all our observations and discuss phenomena potentially responsible for the observed broadening of a Bragg spot. But, in advance, we would like to provide additional practical information, and we present data in Appendix C illustrating the stability of the signal during the data collection. As can be seen from the figures shown in Appendix C, our signal is weakly dependent on the top-up mode on the synchrotron. We investigated the temporal stability of

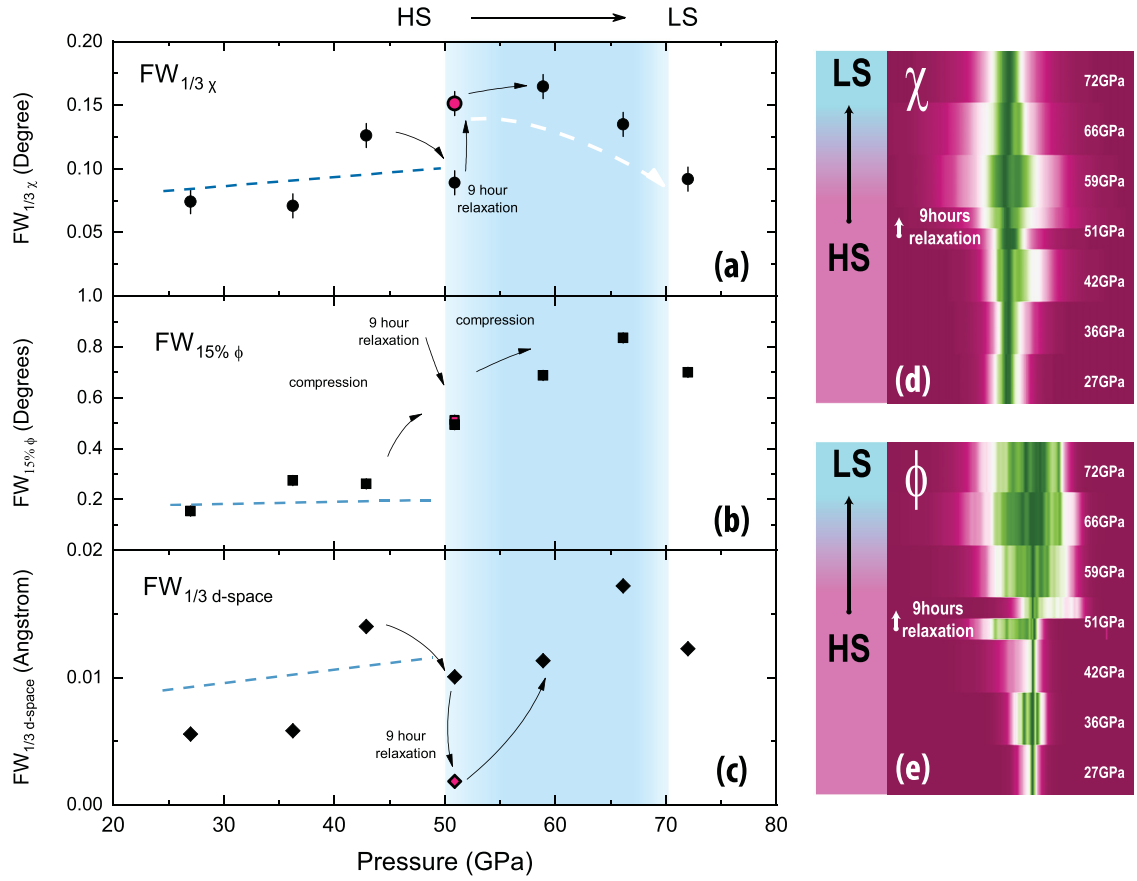

FIG. 7. Variation of Bragg peak $(111)_{hkl}$ FW of Bragg peak projection (a) χ, (b) ϕ, and (c) 2θ under pressure. Note the increase in $FW_{15\%}\phi$ at the pressure range of crossover and reduction of $FW_{1/3}\chi$ at pressures with the sample almost fully transformed into the LS. In the high-resolution regime, the real shape of the sample Bragg peak is intricate, and the correct presentation and analysis of its shape is a complicated task. On the right side, we show 2D color maps of the data shown previously in Figs. 5 and 6 (with peak amplitude normalization) with the bottom axis corresponding to the (d) χ and (e) ϕ values. These images support our considerations concerning the effect of the crossover on the size and the shape of the Bragg peak. For the convenience of the readers, the profiles were offset in order to bring them to a common reference point.

the Bragg spot central slice. We note that the integral intensity of a Bragg spot is constant as well as the corresponding pattern recorded by the detector. The width of the Bragg spot does not change over the time of 80 s of data collection. This test indicates that the timescales of stress-strain relaxation effects described above are significantly longer than the 80 s of the test conducted.

IV. DISCUSSION

Analysis of the unit-cell volume of (Mg,Fe)O as a function of pressure (Figs. 3 and 4) suggests that spin crossover started at 51 GPa, in good agreement with Ref. [13]. We compare the observations extracted from the Bragg peak projections in Fig. 7, and we conclude that $(111)_{hkl}$ Bragg reflection is sensitive to the spin-state crossover from the position and size/shape point of view.

Although effects of spin-state crossover on $FM_{1/3dspace}$ (2θ projection) could be potentially influenced by the effects of stress-strain relaxation described above, variation of $FW_{1/3}\chi$ (χ projection) and $FW_{15\%}\phi$ (ϕ projection) as a function of pressure indicate an obvious response to the crossover. Our observations are supported by the increase in $FW_{1/3}\chi$, especially pronounced after 9-h relaxation at 51 GPa, and a significant increase in $FW_{15\%}\phi$ at the same pressure. At pressure of 72GPa, at the end of the spin-state crossover pressure range, the value of $FW_{1/3}\chi$ decreased to the values preceding the crossover. Please also note that the values of $FW_{15\%}\phi$ start to increase rapidly and become, at least, three times larger if compared to the values preceding the crossover, maintaining these values even after the crossover completion.

The observed behavior of $FW_{1/3}\chi$ can be attributed to additional scattering arising from the appearance of the disorder and competition of HS/LS states. The observation that the maximum of $FW_{1/3}\chi$ corresponds to the middle of the crossover pressure range supports our argument. This pressure region corresponds to the case of 1:1 abundance of HS and LS domains. If the changes in $FW_{1/3}\chi$ would be related with any enhancement of mosaicity in the χ direction, the $FW_{1/3}\chi$ value would not decrease at higher pressures and exhibit the behavior close to that observed for $FW_{15\%}\phi$.

In turn, the changes in $FW_{15\%}\phi$ could be attributed to the defect-structure modification of the material. Within the restriction of fixed sample composition, we may consider formation of stacking faults and/or increased mosaicity of the sample in a specific direction. The scattering geometry

(Fig. 8 of Appendix A) and the data shown in Fig. 6 suggest that the broadening appears in the direction close to being perpendicular to the detector plane. We can add that this is a direction perpendicular to χ projection, and the broadening or shape change occurs parallel or slightly inclined to the vector [111] in the reciprocal space in such way that the Q-scattering vector is constrained.

We observed correlation between microstructure changes in the material and the spin-state crossover and observed it at high pressures on a single crystal. Considering different types of defects, we can exclude formation of uniformly distributed vacancies, in the latter case, we would not see specific directional behavior—the broadening of the Bragg peak would appear in all directions and mostly at the baseline of the Bragg peak. It should also be weak [22].

Taking other effects into account, the formation of stacking faults is one of the most probable explanations for the observed behavior. Stacking faults are considered to be a manifestation of one-dimensional disorder. (MgFe)O is a material with a *fcc* lattice and, thus, may have stacking faults of twin or deformation type [23]. Although the former type of defects lead to a diffraction line broadening, the latter are responsible for effects of a broadening and a line shift. Additional information can be found elsewhere [23].

Another explanation for the observed effect would be a formation of subgrain boundaries leading to a minor rotation of $(111)_{hkl}$ planes around the ϕ axis (see scattering diagrams featured in Figs. 1 and 8 of Appendix A). One can imagine a crystal bending as an example of such a situation. If we consider that HS and LS domains coexist through the bulk of the material homogeneously (with their abundance controlled through the pressure and the temperature), we mark this scenario to be less probable. There is no obvious scenario relevant for the spin-state crossover explaining why mosaicity would evolve in a certain direction, and why it would not evolve at the same time in the χ cross section. We mention the bulk of the material since x-ray diffraction was collected in Laue geometry, and, thus, the scattered signal carries information about the full thickness of the sample. In contrast, stacking faults can be formed locally, and this process seems to be a more logical strain release mechanism for the contact strains appearing due to HS-LS domain interaction. Finally, we add that stacking faults are not an uncommon phenomenon for the rock-salt structures [24–26].

Formation of the stacking faults as planar defects could be correlated with information on the slip planes typical for cubic systems. The main slip systems for our material are $\{110\}(1\bar{1}0)$, $\{100\}(011)$, and $\{111\}(1\bar{1}0)$. Although, the slip systems of $\{100\}(011)$ and $\{111\}(1\bar{1}0)$ were shown to be less probable than $\{110\}(1\bar{1}0)$ as follows from a study employing strongly nonhydrostatic conditions [4], we note that the latter study determined the most probable and dominant slip planes, and, indeed, the less probable $\{111\}(1\bar{1}0)$ slip plane could still be relevant to the behavior attributed to the spin-state crossover.

In order to avoid any confusion, we would like to clarify that the observed broadening attributed to stacking faults would be observed differently for powder and single-crystalline material. In powders, the response is averaged over an ensemble of many grains and numerous orientations, whereas in the case of a single crystal, the effect should be directional. Due to the specific limitations of our experimental setup, we could access only one Bragg peak and could not retrieve additional information, particularly, the orientation matrix of the crystal with respect to the x-ray beam and the compression axis. Finally, one should not consider the picture of defects or stacking faults formation as the only mechanism accommodating the contact strains of HS-LS during the crossover. However, this is the first experimental confirmation (to our knowledge) of such a process. We can mention other examples related to the HS-LS contact strain accommodation which have not yet been given attention from the high-pressure community. They include modification of the Fe^{2+} local crystal structure at the HS-LS boundary changing the local crystal-field configuration and, thus, the electron distribution across different d-electron orbitals. Such effects are very difficult to resolve experimentally in conventional high-pressure x-ray diffraction, x-ray emission spectroscopy, Mössbauer spectroscopy—the techniques commonly used for spin-state investigations. These effects also present a certain challenge to theoretical studies.

All in all, at this point, we can conclude that data collected in the χ projection of the $(111)_{hkl}$ Bragg peak demonstrates additional finite scattering correlated with the disorder caused by the presence of HS and LS. We also report the formation of static structural defects which accumulate as material is transformed domain by domain from HS to LS.

We consider that the discussion would not be complete if we do not address temporal evolution of our signal for the individual slices of the Bragg peak. In the Introduction, we mentioned that, in a situation of spin-state crossover and strongly suppressed kinetics, the system may still breathe by switching HS to LS—the process of small to little energy fluctuation (e.g., temperature). This process could be potentially investigated if we inspect and compare evolution of diffraction spot speckles collected before, during, and after the spin-state crossover as a function of time. Data presented in Appendix C allow us to conclude that, within 80 s of data collection with a frame exposure time of 0.05 s, we do not resolve any additional features which could be attributed to the HS/LS domain fluctuations. If we will slice the Bragg spot at the center and cross correlate variations of different regions of interest with finite intensity, then all the anomalies detected in the temporally resolved signal will be unambiguously attributed to the fluctuations related to the operation of the synchrotron source. This observation indicates that the process of domain breathing is either much faster than the exposure of the frames, and here, we limited by the photon flux, or, which is equally probable, the process is much slower and could be resolved in future studies.

V. CONCLUSION

By using (MgFe)O as an example of a material with strongly correlated properties and with distinct relatively broad spin-state crossover of ferrous iron, we characterize the latter phenomenon using the high-resolution x-ray diffraction under high-pressure conditions.

We select the composition with moderate iron content $x_{Fe} = 0.19(1)$ and focus on the features of the $(111)_{hkl}$ Bragg

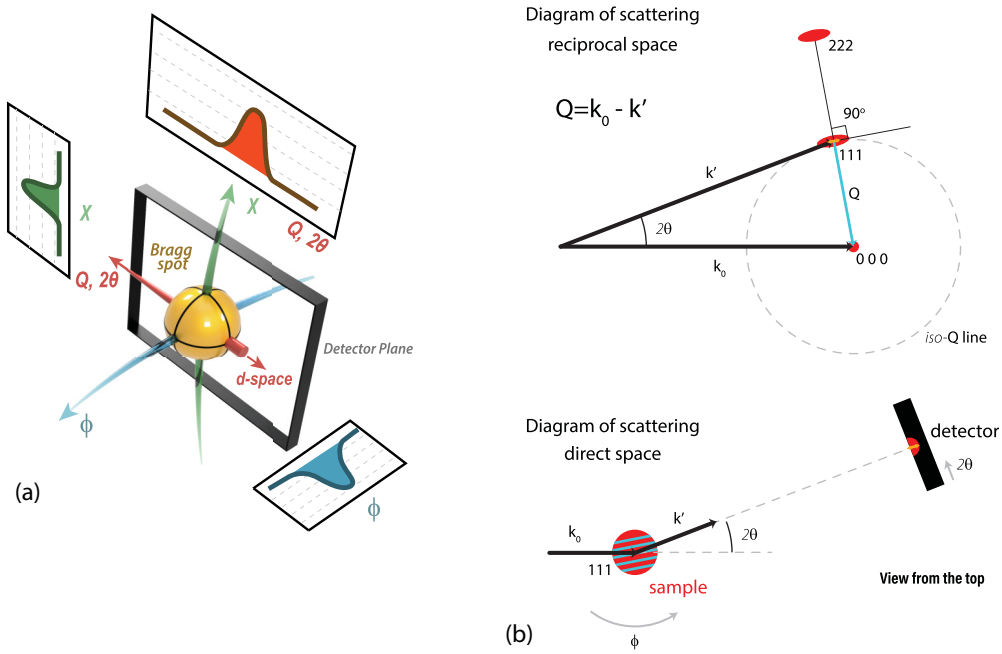

FIG. 8. (a) Basic representation of the experiment and the derived data through individual projections along 2θ, χ, and ϕ. (b) Scattering diagrams describing experiment at the beamline P10. Please see the text for a discussion. The orange line indicates the situation of the Bragg spot broadening in the reciprocal space as detected during ϕ rotation in the direction perpendicular to the plane of the detector.

spot as we approach and pass through the pressure range of coexisting HS/LS states. We find and describe the effects of stress-strain relaxation as well as subtle changes in Bragg spot shape and size, some of those we attribute to the formation of static microstructure defects accumulating during the spin-state crossover in the single-crystal material. We suggest that the formation of microstructural defects is one of intrinsic processes of contact strain relaxation upon the transformation of HS domains to LS.

Finally, even for a composition of $x_{\mathrm{Fe}} = 0.19(1)$, we detect evidences which we describe as the additional contribution to the diffraction signal caused by the presence of intrinsic disorder in the form of HS-LS domains. Indeed, this contribution, manifested through an additional Bragg peak broadening,

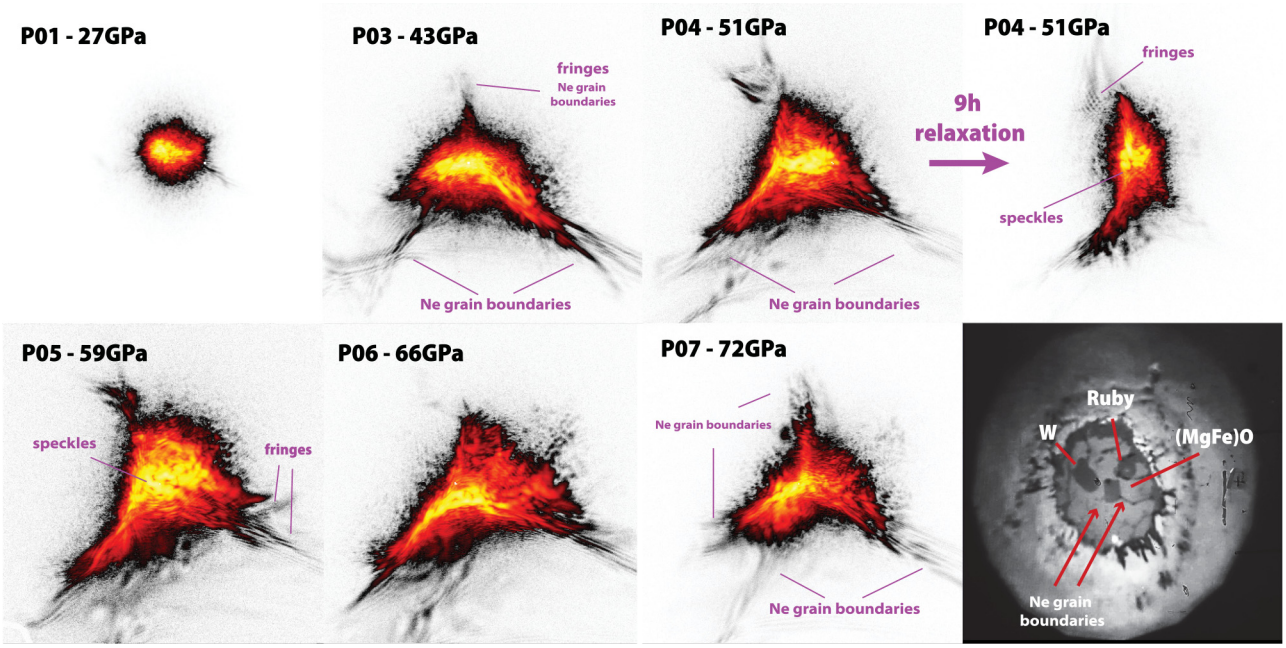

FIG. 9. Central slices of the $(111)_{hkl}$ Bragg spot collected for 80 s together with an illustration of an additional contribution to the diffraction signal.

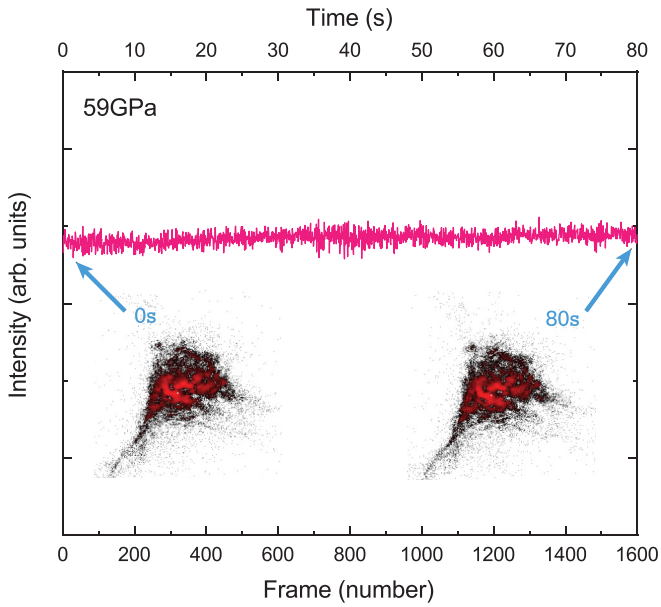

FIG. 10. Stability of the in-frame intensity as a function of time. Data were collected at a selected ϕ angle and represent intensity variation over time for a central slice of the Bragg spot. Within the counting statistics, the Bragg spot image seems the same and not affected by the stress-strain relaxation mentioned above.

reaches maximum at pressures corresponding to the middle of the crossover, and, thus, it corresponds to the equal abundance of the HS and LS.

ACKNOWLEDGMENTS

We acknowledge DESY (Hamburg, Germany), a member of the Helmholtz Association HGF, for the provision of experimental facilities. Parts of this research were carried out at PETRA III, DESY. We acknowledge the Extreme Conditions Science Infrastructure of PETRA III, DESY for their help and access to their visible-light spectroscopic facilities. We acknowledge great help from anonymous reviewers during the preparation of the paper.

APPENDIX A: SCATTERING DIAGRAMS

In Fig. 8, we demonstrate basic scattering diagrams supplementing our discussion on the geometry of the data collection and the Bragg spot, projections, and broadening detected during ϕ rotation. We illustrate the individual projections and the data retrieved from the detector plane. The direction of the χ projection is perpendicular to the diagram plane.

If we would detect a broadening of the Bragg peak in the direction perpendicular to the detector plane in the reciprocal space that would correspond to a change in shape in the [111] vector on a tangent to the iso-Q surface.

APPENDIX B: INTEGRAL INTENSITIES OF THE $(111)_{hkl}$ BRAGG SPOT

See Fig.9 for a diagram of the central slices of the $(111)_{hkl}$ Bragg spot.

APPENDIX C: TEMPORAL PROPERTIES OF THE BRAGG SPOT

In Fig. 10, we present our measurements of the frame total intensity stability as a function of time. It indicates that the section of the (MgFe)O $(111)_{hkl}$ Bragg spot was not considerably changing during 80 s of collection time.

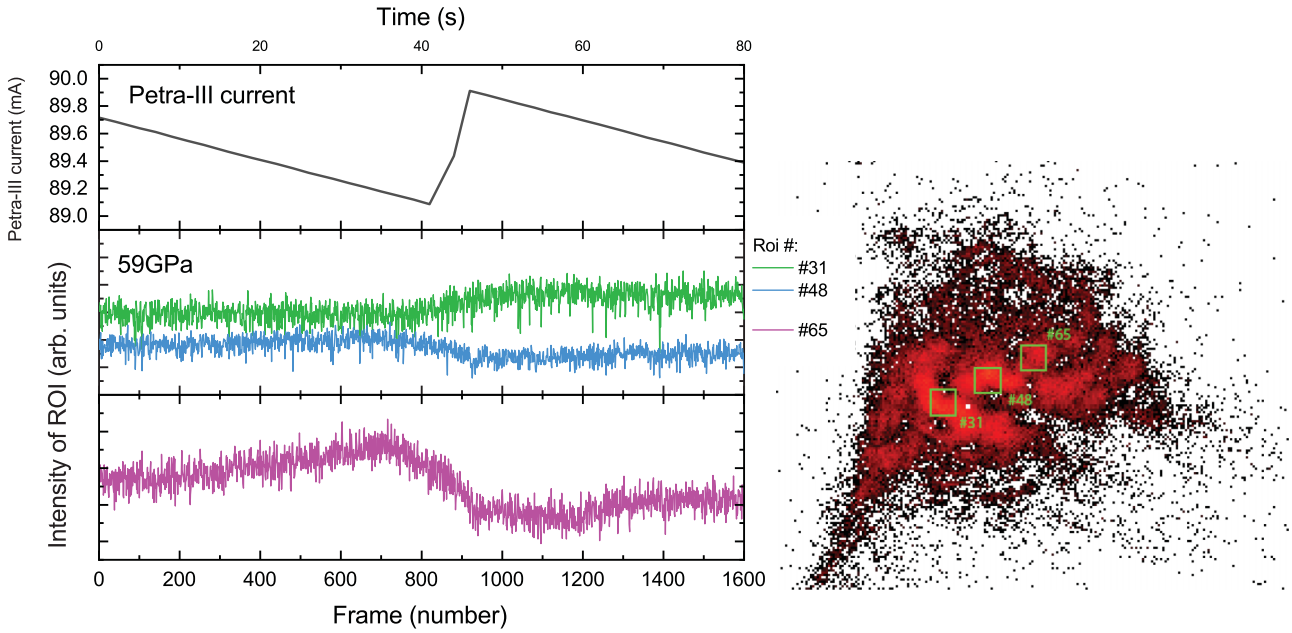

FIG. 11. Variation of selected speckle intensities (numbered regions of interest for the Bragg spot shown on the right) as a function of time. Data are shown in correlation with the Petra III current change. Data were collected at a specific ϕ angle and represent a central slice of the $(111)_{hkl}$ Bragg spot collected at pressures close to the middle of the HS-LS crossover.

In addition, we would like to mention importance of the synchrotron source stability on the measurements. This is indicated in Fig. 11 where we compare the intensity of selected speckles as a function of time in correlation with the Petra-III synchrotron current in the 1% top-up mode. One can see a small variation of intensity related with the synchrotron bunch refilling procedure related (as we suggest) with small angular deviations of the incident beam falling on the sample. These small deviations did not affect our data on the widths of the Bragg spot.

[1] J.-F. Lin, S. Speziale, Z. Mao, and H. Marquardt, Rev. Geophys. **51**, 244 (2013).

[2] J. Badro, Annu. Rev. Earth Planet. Sci. **42**, 231 (2014).

[3] J. M. R. Muir and J. P. Brodholt, Earth Planet. Sci. Lett. **417**, 40 (2015).

[4] J. Immoor, H. Marquardt, L. Miyagi, F. Lin, S. Speziale, S. Merkel, J. Buchen, A. Kurnosov, and H. P. Liermann, Earth Planet. Sci. Lett. **489**, 251 (2018).

[5] E. Dagotto, Science, **309**, 257 (2005).

[6] A. I. Nesterov, Y. S. Orlov, S. G. Ovchinnikov, and S. V. Nikolaev, Phys. Rev. B **96**, 134103 (2017).

[7] A. I. Nesterov and S. G. Ovchinnikov, JETP Lett. **90**, 530 (2009).

[8] W. Cota, G. Ódor, and S. C. Ferreira, Sci. Rep. **8**, 9144 (2018).

[9] E. Dagotto, New J. Phys. **7**, 67 (2005).

[10] Z. Mao, J.-F. Lin, J. Liu, and V. B. Prakapenka, Geophys. Res. Lett. **38**, L23308 (2011).

[11] D. Yamazaki and T. Irifune, Earth Planet. Sci. Lett. **216**, 301 (2003).

[12] K. K. Zhuravlev, J. M. Jackson, A. S. Wolf, J. K. Wicks, J. Yan, and S. M. Clark, Phys. Chem. Miner. **37**, 465 (2010).

[13] K. Glazyrin, R. Sinmyo, E. Bykova, M. Bykov, V. Cerantola, M. Longo, C. McCammon, V. B. Prakapenka, and L. Dubrovinsky, Phys. Rev. B **95**, 214412 (2017).

[14] I. Kantor, L. Dubrovinsky, C. McCammon, G. Steinle-Neumann, A. Kantor, N. Skorodumova, S. Pascarelli, and G. Aquilanti, Phys. Rev. B **80**, 014204 (2009).

[15] H.-P. Liermann, Z. Konôpková, W. Morgenroth, K. Glazyrin, J. Bednarčik, E. E. McBride, S. Petitgirard, J. T. Delitz, M. Wendt, Y. Bican, A. Ehnes, I. Schwark, A. Rothkirch, M. Tischer, J. Heuer, H. Schulte-Schrepping, T. Kracht, and H. Franz, J. Synchrotron Radiat. **22**, 908 (2015).

[16] C. S. Zha, H. Mao, and R. J. Hemley, Proc. Natl. Acad. Sci. USA **97**, 13494 (2000).

[17] S. Speziale, C.-S. Zha, T. S. Duffy, R. J. Hemley, and H. Mao, J. Geophys. Res.: Solid Earth **106**, 515 (2001).

[18] S. D. Jacobsen, C. M. Holl, K. A. Adams, R. A. Fischer, E. S. Martin, C. R. Bina, J.-F. Lin, V. B. Prakapenka, A. Kubo, and P. Dera, Am. Mineral. **93**, 1823 (2008).

[19] H. Marquardt, S. Speziale, K. Marquardt, H. J. Reichmann, Z. Konôpková, W. Morgenroth, and H. P. Liermann, J. Appl. Phys. **110**, (2011).

[20] K. Glazyrin, N. Miyajima, J. S. Smith, and K. K. M. Lee, J. Geophys. Res.: Solid Earth **121**, 3377 (2016).

[21] Z. Jenei, H. P. Liermann, R. Husband, A. S. J. Méndez, D. Pennicard, H. Marquardt, E. F. O'Bannon, A. Pakhomova, Z. Konopkova, K. Glazyrin, M. Wendt, S. Wenz, E. E. McBride, W. Morgenroth, B. Winkler, A. Rothkirch, M. Hanfland, and W. J. Evans, Rev. Sci. Instrum. **90**, 065114 (2019).

[22] J. D. Makinson, J. S. Lee, S. H. Magner, R. J. De Angelis, W. N. Weins, and A. S. Hieronymus, Adv. X-Ray Anal. **42**, 407 (2000).

[23] R. Berliner and S. A. Werner, Phys. Rev. B **34**, 3586 (1986).

[24] G. Fontaine, J. Phys. Chem. Solids **28**, 2553 (1967).

[25] P. W. Tasker and T. J. Bullough, Philos. Mag. A **43**, 313 (1981).

[26] M. T. Sprackling, J. Photogr. Sci. **32**, 21 (1984).